

Copyright © 1982, by the author(s).  
All rights reserved.

Permission to make digital or hard copies of all or part of this work for personal or classroom use is granted without fee provided that copies are not made or distributed for profit or commercial advantage and that copies bear this notice and the full citation on the first page. To copy otherwise, to republish, to post on servers or to redistribute to lists, requires prior specific permission.

AXIAL PLASMA INJECTION AND SHOCK FORMATION  
IN MULTIPLE MIRRORS

by

R.V. Bravenec, A.J. Lichtenberg, and M.A. Lieberman

Memorandum No. UCB/ERL M82/68

14 June 1982

ELECTRONICS RESEARCH LABORATORY  
College of Engineering  
University of California, Berkeley  
94720

## Axial plasma injection and shock formation in multiple mirrors

R.V. Bravenec<sup>a)</sup>, A.J. Lichtenberg, and M.A. Lieberman

Department of Electrical Engineering and Computer Sciences  
and Electronics Research Laboratory, University of California,  
Berkeley, California 94720

The axial injection of a high-beta collisional plasma from a conical theta-pinch source into a multiple-mirror device and its subsequent thermalization due to shock formation is investigated numerically and experimentally. An ideal-fluid Lagrangian simulation is developed and used to study plasma expansion from the theta-pinch into a solenoidal field. Expansion into multiple mirrors is then examined. Shocks are found to form sequentially in the mirror throats, beginning with the mirror nearest the theta-pinch; these propagate upstream and thermalize the drift energy. The shocks form later in time as the mirror fields are reduced, until a minimum field is reached below which shocks do not form. Experimental results are presented (temperatures of 6-15 eV, densities of  $10^{14}$  -  $10^{15}$   $\text{cm}^{-3}$ ) which verify the predictions of the simulations. The observation that quadrupole stabilization fields interfere with shock thermalization is discussed.

PACS numbers: 52.30+r, 52.35.Tc, 52.55.Ke, 47.60.+i

---

<sup>a)</sup> Present address: Fusion Research Center, University of Texas, Austin, Texas 78712.

## I. INTRODUCTION

The process by which plasma may be injected axially and efficiently trapped in a magnetic mirror machine or set of multiple mirrors is of interest for many laboratory experiments. Frequently the plasma is so collisional that shock formation in the mirror throats is the dominant thermalization mechanism for single-ended injection. Much experimental<sup>1-3</sup>, theoretical<sup>4,5</sup> and numerical<sup>5</sup> work has been performed investigating shock-thermalization of plasma flow by a single mirror. Although plasma trapping in mirror machines by shock formation has been studied experimentally<sup>6</sup>, little theoretical or numerical work exists. The purpose of this work is to investigate, via a numerical fluid simulation and related experiments, plasma expansion from a conical theta-pinch into a multiple-mirror device and subsequent plasma trapping. The plasma studied is of high beta (the ratio of plasma pressure to vacuum magnetic field pressure).

Section II presents a description of the experimental apparatus. Section III describes the fluid simulation code. The code is first used to study the scaling of plasma parameters - density, temperature, drift velocity, etc. - for plasma injection into a uniform solenoid (a mirror ratio  $R_m$  of unity) as the ratio of solenoidal field to peak theta-pinch field  $b_S$  is varied. Then, a solution for injection into multiple mirrors with  $R_m = 4$  is presented, which points out the features of shock formation and thermalization. A study is presented of the dependence of the shock formation time in the first mirror as a function of the "machine parameters"  $R_m$  and  $b_S$ . The predictions of the simulations are compared with experiments in Section IV; the experiments are performed both with and without quadruple stabilizing fields for  $R_m > 1$ .

## II. THE EXPERIMENTAL APPARATUS

The experimental apparatus can be divided into three major sections: (1) the multiple-mirror device, (2) the conical theta-pinch plasma source, and (3) the guide-field region. A scale drawing of the experiment, showing only a portion of the multiple-mirror device, is given in Fig. 1.

The magnetic field of the multiple-mirror device is generated by four independent magnet systems. A solenoid consists of an approximately 8-m long series of linked current loops. A set of eleven magnetic mirror coils of average radius 6.85 cm are spaced by a "cell length"  $\ell_c$  of 75 cm. The remaining magnets are sets of linked Ioffe bars which alternate current directions from cell to cell. To achieve minimum-average-B stability, there are two separate quadrupole-coil systems.<sup>7</sup> There are four separate capacitor banks which power the coils. Each is fired at such a time that all fields peak together, and each bank is then crowbarred. The L/R decay times are all approximately 2 msec, which is sufficiently long for the fields to be considered constant in the experiments to be discussed. The vacuum chamber is primarily made of sections of 3.5-in. i.d., 50-mil wall stainless steel tubing. These sections are joined in each midplane with short glass sections having four access ports each. The base pressure of the system is  $\sim 10^{-6}$  Torr. It is useful to define a nomenclature for the various port positions: The mirrors are numbered from the theta-pinch end starting with 0 and are denoted by  $T_0, T_1, T_2$ , etc. (T standing for "throat"), as in Fig. 1. The midplane ports (glass sections) are denoted by  $M_{01}, M_{12}, M_{23}$ , etc. (i.e., the midplane ports between  $T_0$  and  $T_1$ , etc.), as in Fig. 1. The three pumping ports are at  $M_{01}, M_{45}$ , and  $M_{89}$ .

A theta-pinch device was chosen for its ability to produce a high-

beta, relatively clean plasma. A fast capacitor bank is discharged through a single-turn conical coil surrounding the vacuum chamber in which hydrogen gas is transiently admitted. The axial pressure of the resulting plasma drives an expansion centered about the location of peak magnetic field. For a conically shaped coil, this location is near one end of the coil, and the expansion is largely directed toward the other end. The coil is of minimum inner radius 3.7 cm, maximum inner radius 6.8 cm ( $6^\circ$  cone angle), and length 30 cm. A cross section is shown as the dotted lines in Fig. 2 along with the calculated (dashed curve) and measured (solid curve) magnetic field profiles. The calculated profile was obtained by assuming that the current distribution lies on the inner surface of the coil and varies as  $r_i^{-2}$ , where  $r_i(z)$  is the inner radius of the coil. In order to take advantage of the increasing azimuthal electric field with radius, the quartz discharge chamber is also conical and fitted to within 1/4 in. of the coil. Hydrogen is injected into the chamber at a point just behind the coil by an electromechanical "puff valve", indicated in Fig. 1.

The theta-pinch may be operated in a ringing mode or a preionized/crowbarred mode with a variable number  $N_{PB}$  of 2.1- $\mu$ F, 50-kV primary-bank capacitors. For producing large quantities of relatively cool plasma, the former is used because of its simplicity and reliability. For a hotter, cleaner plasma, the latter mode is required. The pieionizer consists of a 0.4- $\mu$ F, 125-kV capacitor charged to 60 kV which is discharged through the coil just prior to primary-bank firing. Discharge waveforms, obtained with a pickup coil located in the fringing fields of the theta-pinch coil, are shown in Fig. 3 for (a) ringing and (b) preionized/crowbarred operation. Here,  $N_{PB}=3$  and the delay between puff-value and theta-pinch triggering  $t_d$  was 300  $\mu$ sec. (The significant modulation of the crowbarred current is due to the low inductance of

the theta-pinch coil relative to that of a single crowbar spark gap.)

In order to isolate the multiple-mirror device from the neutral gas injected by the puff valve, the theta-pinch and the multiple-mirror device are separated by a guide-field solenoid of length 138 cm. A special set of quadrupoles is used to map an elliptical flux surface in the first mirror throat (when the strong and/or weak quadrupoles are energized) back to a circle near the theta-pinch. For the experiments in Section IV, the guide field is set equal to the solenoid field. As shown in Fig. 1, the windings of the guide-field solenoid are spread apart at two locations denoted by  $M_{B0}$  and  $M_{AB}$  (75 cm and 150 cm from  $M_{01}$ , respectively) to accommodate two port sections. An iris aperture having minimum and maximum openings of 0.45 cm and 5.9 cm, respectively, and capable of being adjusted while under vacuum is located about 15 cm downstream of  $M_{AB}$ , shown in Fig. 1. For the experiments to be discussed, the aperture is set fully open.

The experimental data was obtained with Langmuir probes,<sup>8</sup> a triple-probe<sup>9</sup>, compensated diamagnetic loops<sup>10</sup>, and a "velocity-stagnation probe." The Langmuir probes, each consisting of 40-mil exposed lengths of 5-mil tungsten wire, are biased at -50V to collect ion saturation current, from which the plasma density is inferred. The triple-probe consists of three identical Langmuir probes in close proximity; two of the probes are biased with respect to each other, with one in ion saturation, and form a standard floating double-probe<sup>8</sup>, while the third probe floats. The current of the biased pair provides a measure of the plasma density while the voltage between the positively-biased probe of the pair and the floating probe is proportional to the electron temperature. The contribution of plasma drift to the Langmuir-probe and triple-probe currents is approximated by the expression

$I = (I_i^2 + I_d^2)^{1/2}$ , where  $I_i$  is the thermal ion saturation current given by Lafromboise<sup>11</sup>, and  $I_d = nevA'_p$ , where  $A'_p$  is the probe area projected in the direction of flow. The velocity-stagnation probe is a relatively small gridded electrostatic analyzer oriented such that the entry grid faces away from the theta-pinch. To avoid drastically disturbing the plasma, the device is located approximately 2 cm off axis. Inside, a collector plate is biased at -50V with respect to the floating case. When the drift velocity is significant, no current is collected since the entry grid is in the wake of the flow. Otherwise, ions are collected; a pulse of current then indicates an abrupt halting of the flow, as after passage of a shock. Prior to this time, drift velocity is obtained using time of flight from the theta-pinch. The compensated diamagnetic loops, indicated in Fig. 1 as  $DL_A$ ,  $DL_{01}$ , and  $DL_{12}$ , each consists of a coil wrapped around the vacuum chamber in series with another coil over the first with twice the area and half the number of turns, such that the vacuum signals vanish. With plasma present, the integrated output voltage is proportional to the plasma pressure (beta) averaged over the chamber cross section (for  $\beta \lesssim 0.5$ ).  $DL_{01}$  and  $DL_{12}$  each have four inner turns while  $DL_A$  has two. The effects of the metallic vacuum chamber on the loop signals are corrected using a minor change in the passive integrating circuitry.<sup>12</sup>

### III. FLUID SIMULATION OF PLASMA INJECTION

#### A. Description of the computer code

An ideal-fluid analysis incorporating high beta is performed based on the equations of Hamada et al.<sup>5</sup> These consider an azimuthally symmetric plasma column in which transport across the magnetic field is neglected. A paraxial approximation is made for which the radial flow

velocity is much less than the axial velocity. The equations of force, energy, and continuity are then, respectively,

$$nm_i \frac{dv}{dt} = -2 \frac{\partial}{\partial z} (nkT), \quad (1a)$$

$$\frac{dT}{dt} = -\frac{2}{3} T \left( \frac{\partial v}{\partial z} + \frac{1}{A} \frac{dA}{dt} \right), \quad (1b)$$

$$\frac{dn}{dt} = -n \left( \frac{\partial v}{\partial z} + \frac{1}{A} \frac{dA}{dt} \right), \quad (1c)$$

where  $d/dt \equiv \partial/\partial t + v\partial/\partial z$ ,  $z$  is the coordinate along the magnetic field,  $n$  is the ion (singly charged) and electron density,  $A$  is the plasma cross section,  $v$  is the flow velocity along the field,  $T$  is the common ion and electron temperature,  $m_i$  is the ion mass, and  $k$  is Boltzmann's constant. In addition, we use the equations of magnetic flux conservation, radial pressure balance, and the definition of plasma beta, respectively given by

$$\frac{d}{dt}(AB_i) = 0, \quad (2a)$$

$$2nkT + \frac{B_i^2}{2\mu_0} = \frac{B_e^2}{2\mu_0}, \quad (2b)$$

$$\beta \equiv 2nkT \left( \frac{B_e^2}{2\mu_0} \right)^{-1}, \quad (2c)$$

where  $B_i$  and  $B_e$  are the magnetic fields respectively internal and external to the plasma column and  $\mu_0$  is the permeability of free space.

Equations (2a)-(2c) can be combined to yield

$$\frac{1}{A} \frac{dA}{dt} = - [B_e(1-\beta)^{1/2}]^{-1} \frac{d}{dt} [B_e(1-\beta)^{1/2}]. \quad (1d)$$

The adiabatic Mach number is defined by  $M \equiv v/v_s$ , where  $v_s \equiv [2(5/3)T/m_i]^{1/2}$  is the adiabatic sound speed.

Equations (1a)-(1d) are a set of four equations in the four unknowns  $n, T, v$ , and  $A$  in terms of the known external magnetic field  $B_e(z)$ .  $B_e(z)$  is taken to model the magnetic field of the experiment at the time of peak theta-pinch current, as in Fig. 4. Here, the solid and dashed profiles represent the cases  $R_m = 4$  and  $R_m = 1$ , respectively. In both cases  $b_s$ , defined as the ratio of solenoid (and guide) field to peak theta-pinch field, is 0.2. The location  $z/l_c = 0$  is taken to correspond to the first mirror throat ( $T_0$ ), such that the location of the theta-pinch field maximum is  $z/l_c = -2.5$ .

Following the procedure of Hamada et al., Eqs. (1a)-(1d) are rewritten in a Lagrangian frame (moving with the fluid) and solved numerically for a plasma initially at rest and localized entirely within the theta-pinch region. The initial profiles of  $n$  and  $T$  decrease monotonically from  $n_0$  and  $T_0$  at  $z/l_c = -2.5$  to zero at the plasma-vacuum interface  $z/l_c = -2.5 + \zeta_1$ . In the following solutions, the normalized axial extent of the initial plasma,  $\zeta_1$ , is chosen to be 0.4, such that the interface lies roughly at the front of the theta-pinch coil. The initial beta and temperature profiles are chosen to be approximately uniform over most of the plasma. The boundary conditions are chosen to be  $v=0$  at  $z/l_c = -2.5$  (by symmetry as  $\partial B_e/\partial z = 0$  there) and  $T=0$  at the plasma-vacuum interface (a simplified statement of a vanishing force density there).

In order to deal with shocks, an artificial viscosity introduced by VonNeumann and Richtmyer<sup>13</sup> is employed. The resulting system of equations is solved using the packaged partial differential equation solver

PDECOL<sup>14</sup> as the core of a controlling and diagnostic code. Details of  $B_e(z)$ , the solution scheme, and the initial conditions are found in Ref. 12.

Before presenting numerical solutions, the differences between the present formulation and that of Hamada et al. should be pointed out. They considered uniform initial conditions in a uniform theta-pinch field enabling them to base their formulation on the problem of an ideal gas localized at one end of an otherwise evacuated tube by a diaphragm which is subsequently ruptured.<sup>15</sup> They chose as a boundary condition at the plasma-vacuum interface the theoretically derived escape-front velocity  $v_E \equiv [2/(\gamma-1)]v_{s0}$ , where  $\gamma = 5/3$  and  $v_{s0}$  is the sound speed in the undisturbed gas. In the present formulation, such a choice is inappropriate because the nonuniformities in the initial conditions do not allow a theoretical determination of the escape-front velocity. Instead, the escape front is allowed whatever velocity is consistent with a vanishing force density.

Before proceeding with a study of flow through multiple-mirrors, it is worthwhile to examine the expansion of the plasma from the theta-pinch into only the solenoid field.

#### B. Solutions for $R_m = 1$

A numerical solution for  $b_S = 0.2$  and  $\beta_0 = 0.9$  is presented in Fig. 5. Spatial profiles of  $n/n_0$ ,  $T/T_0$ ,  $\beta$  and  $v/v_{i0}$  where  $v_{i0} = (2kT_0/m_i)^{1/2}$ , are presented at normalized time intervals of  $t/t_c = 0.25$  in Fig. 5 ( $t_c \equiv l_c/v_{i0}$ ). The dotted curves in the plots of  $v/v_{i0}$  are graphs of  $v_s/v_{i0} = (5T/3T_0)^{1/2}$ , the normalized sound speed; the dots are Lagrangian grid points and represent fluid elements.

It is evident from the first "snapshot" at  $t/t_c = 0.25$  that the flow has become predominantly supersonic with a nearly linear velocity

profile behind the escape front, as in the results of Hamada et al. As time progresses, the escape-front velocity slowly increases, surpassing the value  $v_E$ , and maxima develop in the profiles of  $n$ ,  $T$ , and  $\beta$  downstream of the theta-pinch. These results, which differ from those of Hamada et al., are due to the stronger pressure gradients which empty the present theta-pinch faster than that of Hamada et al. This is evident by the steeper slope of  $v(z)$  in the theta-pinch region than elsewhere. General observations are the following: The decay of  $n$  and  $T$  is initially rapid (especially  $n$ ) because of the radial expansion of the plasma upon exiting the theta-pinch. (Note the scale change in the plot of  $n/n_0$  at  $t/t_c = 0.75$ .) This does not apply to  $\beta$  since the drop in  $B_e$  partially cancels the decay of the product  $nT$ . At later times the decay of  $n$ ,  $T$ , and  $\beta$  is governed by axial expansion. Provisions exist in the code to monitor the fluid parameters versus time at a fixed position ("probe traces"). Results at  $z/l_c = 0.5$  (the midplane of the first mirror cell) for the solution just discussed are shown in Fig. 5(b). Although the Mach number, given by the ratio of the curves  $v/v_{i0}$  and  $v_s/v_{i0}$ , is seen to decay monotonically at a given position, the flow never becomes subsonic; hence, no shocks form and the flow velocity is never thermalized.

To investigate the scalings of  $n$ ,  $T$ ,  $\beta$ , and  $v$  with  $b_s$  (and  $\beta_0$ ), a series of runs is made for all combinations of the values  $b_s = 0.1, 0.2, 0.3$ , and  $\beta_0 = 0.0, 0.5, 0.9, 0.99$ . The normalized quantities  $\tau_{\beta\max}$ ,  $\eta_{\beta\max}$ ,  $T_{\beta\max}$ ,  $\beta_{\max}$ ,  $V_{\beta\max}$ , and  $M_{\beta\max}$  at  $z/l_c = 0.5$  are plotted versus  $b_s$  with  $\beta_0$  a parameter in Fig. 6. Here  $\tau \equiv t/t_c$ ,  $\eta \equiv n/n_0$ ,  $T \equiv T/T_0$ , and  $V \equiv v/v_{i0}$ , and the subscript  $\beta_{\max}$  denotes the quantity at the time of peak beta. (For  $\beta_0 = 0$ ,  $\tau_{\beta\max}$  is defined as the average of the times when  $\eta$  and  $T$  reach their maxima.) First, it is evident that  $\tau_{\beta\max}$  and  $V_{\beta\max}$  are

closely related; in fact, the normalized "time-of-flight" velocity  $V_{\text{tof}} \equiv 3/\tau_{\beta_{\text{max}}}$  agrees closely with  $V_{\beta_{\text{max}}}$ -- the true normalized flow velocity. This result is useful in a practical sense, since the former is much easier to measure in the laboratory. For moderate values of  $\beta_0$ , both velocities increase slightly with  $b_S$ , in agreement with the experimental results of Waelbroeck et al.<sup>10</sup> This can be understood from the plot of  $T_{\beta_{\text{max}}}$  in which the temperature is seen to increase with  $b_S$ : because of equipartition, more energy is then available for the drift. However, for  $\beta_{\text{max}} \rightarrow 1$ , the flow velocity drops with  $b_S$  as exemplified by the case  $\beta_0 = 0.99$ --this is presumably a result of the increasing field that the plasma must push aside.

The increases in  $\eta_{\beta_{\text{max}}}$  and  $T_{\beta_{\text{max}}}$  with  $b_S$  are results of reduced radial decompression upon exiting the theta-pinch. The increases with  $\beta_0$  are due to essentially the same effect--by Eq. (1d), the increase in the cross section of a fluid element in dropping to a lower field is reduced by the factor  $[(1-\beta)/(1-\beta_0)]^{1/2}$ . Empirically,  $T_{\beta_{\text{max}}}$  of Fig. 6 scales roughly as  $b_S^{1/2}$ , and  $\eta_{\beta_{\text{max}}}$  scales somewhat slower than  $T_{\beta_{\text{max}}}^{3/2} \propto b_S^{3/4}$  (except in the case  $\beta_0 = 0.99$ ). Because the increase in the product  $\eta_{\beta_{\text{max}}} T_{\beta_{\text{max}}}$  is less than that of  $b_S^2$ ,  $\beta_{\text{max}}$  is seen to decrease with  $b_S$ . The extreme nature of the case  $\beta_0 = 0.99$  is clear in the fact that  $\beta_{\text{max}}$  decays very little for  $b_S = 0.1$  or  $0.2$ , implying that as  $\beta \rightarrow 1$ ,  $\beta_{\text{max}}$  remains constant during the flow. This is a consequence of the magnetic pressure of the strongly distorted field, which constrains the plasma from expanding axially. Using the results for  $V_{\beta_{\text{max}}}$  and  $T_{\beta_{\text{max}}}$ , the Mach number is also plotted in Fig. 6. Unlike  $V_{\beta_{\text{max}}}$ ,  $M_{\beta_{\text{max}}}$  decreases monotonically with increasing  $b_S$  or  $\beta_0$ .

The quantitative features of Fig. 6 are of course particular to the location of the "probes" and to the initial conditions. Choice of the

axial extent of the initial plasma has a strong effect on the quantitative nature of the probe traces although the qualitative features are the same. It is found that halving  $\zeta_1$  roughly halves the peak values of  $\eta$ ,  $T$ , and  $\beta$ . This is understandable, since at any given time the plasma has undergone roughly twice as much axial expansion. The drift velocity is changed only minimally; as a consequence, the Mach number increases as  $\zeta_1$  decreases.

### C. Solutions for $R_m > 1$

From the results of the last section, much can be said about the initial phases of the flow through a multiple-mirror system. It is evident that the velocity of the forward portion of the flow is sufficiently large for a fluid element to traverse a mirror scale length before the macroscopic profiles change significantly. Thus, the flow through a mirror is quasi-static and steady-state equations may be used. From Eqs. (1a)-(1d) with  $\partial/\partial t = 0$ , one obtains

$$v^2 + 5 \left[ \left( \frac{v_0}{av} \right)^{2/3} - 1 \right] = v_0^2, \quad (3a)$$

$$(na)^2 - 5 \left( \frac{an}{v_0} \right) (\eta^{2/3} - 1) = 1, \quad (3b)$$

where the subscript 0 now denotes values at the entry to the mirror where the flow quantities are normalized. For  $v_0 \gg 1$ , one obtains  $v \cong v_0$  and  $\eta \cong a^{-1}(T \cong a^{-2/3})$ . Thus, in the forward portions of the flow, the velocity is relatively unperturbed by the mirrors while the density and temperature rise by roughly the factors  $R_m$  and  $R_m^{2/3}$ , respectively. The plasma beta, which scales as  $nTA^2$ , then decreases only by the factor  $R_m^{1/3}$ . As time progresses, the flow velocity at a given position decays, seen in Fig. 5(b); this effect is accentuated in the mirrors where, by Eqs. (3a) and (3b),  $v$  decays faster than  $v_0$ .

Likewise, the relative increases in  $n$ ,  $T$ , and  $v_s$  in the mirrors become greater as  $v_0$  decays. Thus, it is possible for the mirrors to drive the flow subsonic, producing shocks and thermalizing the flow energy. Since the velocity profiles monotonically increase in  $z$ , as seen in Fig. 5(a), this will first occur in the mirror farthest upstream ( $T_0$ ).

To be more quantitative, a numerical solution with  $R_m = 4$  is presented in Fig. 7, where, as in Fig. 5,  $b_s = 0.2$  and  $\beta_0 = 0.9$ . The first "snapshot" in Fig. 7(a), in which the flow has encountered the first mirror ( $T_0$ ), is at  $t/t_c = 0.75$ ; as asserted above, the velocity profile is relatively unperturbed. At  $t/t_c = 1.0$ , the flow has encountered the second mirror ( $T_1$ ); in the first mirror,  $n$  and  $T$  increase by roughly the factors  $R_m = 4$  and  $R_m^{2/3} \cong 2.5$ , respectively, and  $\beta$  dips only slightly, as expected. At  $t/t_c = 1.25$ , the flow has encountered the third mirror ( $T_2$ ); it is evident that the depressions in the velocity profile are progressively larger in the upstream mirrors. At  $t/t_c = 1.5$ , the flow is very nearly sonic in the first mirror, where the relative increases in  $n$  and  $T$  are greater than the factors  $R_m$  and  $R_m^{2/3}$ , respectively, in agreement with the predictions based on Eqs. (3a) and (3b). This is seen to produce a "spike" on the beta profile just upstream of  $z/\lambda_c = 0$ . Between  $t/t_c = 1.5$  and  $t/t_c = 1.75$ , the flow becomes subsonic in the first mirror. (At  $t/t_c = 1.75$ , the shock is not fully formed, as evident in other solutions in which the artificial viscosity is deleted.) At  $t/t_c = 2.0$ , the shock is fully formed and, as time progresses, it propagates upstream, carrying with it abrupt increases in  $n$ ,  $T$ , and  $\beta$  and an abrupt drop in  $v$ . (In fact,  $v$  is seen to reverse direction as the plasma "sloshes" back.)

Comparing the profiles downstream of the first mirror with those of Fig. 5(a) reveals that those of  $n$  and  $\beta$  are reduced in the present case. This is a consequence of the choking of the flow by the shock

upstream of  $T_0$ . Between  $t/t_c = 2.5$  and  $t/t_c = 2.75$ , the flow becomes subsonic in the second mirror and a shock propagates upstream, as before. As expected, this process continues from mirror to mirror. (The numerical solution is terminated at  $t/t_c = 3.0$  because of the spreading of the grid points downstream of  $z/\lambda_c = 0$ , as evident in the dotted profile of  $v_s/v_{i0}$ . This increases the shock thicknesses, as seen in the second shock, rendering quantitative interpretations unjustifiable.) We note that once the flow becomes subsonic in a mirror, it remains exactly sonic in the throat (evidenced by crossing of the curves  $v/v_{i0}$  and  $v_s/v_{i0}$ . Hence, unlike subsonic flow through a mirror, the flow here is choked "from above" rather than "from below." As for  $R_m = 1$ , probe traces at  $z/\lambda_c = 0.5$  are presented in Fig. 7(b). Comparison with Fig. 5(b) up to the times of the maxima of  $n$ ,  $T$ , and  $\beta$  reveals that the profiles are very similar. However, the profiles of  $n$ ,  $T$ , and especially  $\beta$  are seen to decay more rapidly in Fig. 7(b), a consequence of the choking of the flow by the first shock. For the reasons mentioned earlier, the numerical solution could not be run long enough for the second shock to reach the probes.

As in Fig. 5, the specifics of the solution shown in Fig. 7 depend on the choices for  $b_S$ ,  $\beta_0$ , and, here,  $R_m$ . For the values used in Fig. 7, a shock forms at  $T_0$  very early, such that much of the plasma is prevented from entering the device. (This fact is not altogether bad since, at later times, the shock at  $T_0$  can turn back cold, contaminated plasma. In contrast, for sufficiently small mirror fields it is anticipated that shocks do not form until much of the plasma has escaped the device. It is of interest then to study the time of shock formation as a function of the machine parameters  $b_S$  and  $R_m$ .

Numerically determined values of  $\tau_s$  (defined as the normalized time at which the flow becomes sonic at  $T_0$ ) are plotted versus  $b_s$  in Fig. 8 for  $\beta_0 = 0$  and  $\beta_0 = 0.9$  and for  $R_m =$  (a) 2, (b) 3, and (c) 4. (Since the shock is not fully developed at  $\tau_s$ , the artificial viscosity is not employed; this ensures that  $\tau_s$  is not reduced by this term.) The dashed lines in Fig. 8 represent values of  $b_s$  for which shocks do not form (at least not before  $t/t_c = 8$ , when the plasma has essentially escaped from the device). The sharp "knees" of the curves near these values of  $b_s$ , especially for  $\beta_0 = 0.9$ , indicate a "cutoff" in the shock-formation process, in agreement with the theoretical results of Hamada et al., who demonstrated that solutions exist without shocks for sufficiently small  $R_m$  and large  $M$ . This effect is not dependent on just the relative mirror strength  $b_m \equiv R_m b_s$ , as is evident in Fig. 8 in which the case  $R_m = 2$ ,  $b_s = 0.2$  leads to a shock while the case  $R_m = 4$ ,  $b_s = 0.1$  does not. This is presumably a result of the larger value of  $M$  in the latter case, as seen in Fig. 6. For  $b_s$  above the "cutoff" values,  $\tau_s$  is seen to decrease smoothly with  $b_s$ .

For fixed values of  $b_s$  and  $\beta_0$ ,  $\tau_s$  decreases as  $R_m$  increases. This is due simply to the elevation in temperature, and hence in the sound speed, in the mirrors, which locally decreases the Mach number and allows for a quicker transition to subsonic flow. For fixed values of  $b_s$  and  $R_m$ ,  $\tau_s$  decreases dramatically as  $\beta_0$  increases from 0 to 0.9. In fact, in the latter case,  $\tau_s$  becomes relatively independent of  $b_s$  (above cutoff, of course). This strong dependence on  $\beta_0$  is also a consequence of the increase in temperature with  $\beta_0$ , as is evident in Fig. 6. Finally, we note that  $\tau_s$  asymptotes to a minimum value with increasing  $R_m$  and  $\beta_0$ , as it must since the escape front does not arrive at  $T_0$  until  $t/t_c \approx 0.75$ .

#### IV. EXPERIMENTAL RESULTS

##### A. Injection into a solenoid ( $R_m = 1$ )

The purpose of these experiments was to investigate the scaling of plasma parameters with  $N_{PB}$ , the number of energized theta-pinch primary bank capacitors, at a constant solenoid field of approximately 0.18T. The studies were performed with the theta-pinch operated in the preionized/crowbarred mode.

Oscilloscope traces of the outputs of diamagnetic loop  $DL_{01}$  and a Langmuir probe at  $M_{01}$  are presented in Fig. 9(a) for  $t_d = 300 \mu\text{sec}$ , and the outputs of  $DL_{01}$  and the triple-probe at  $M_{01}$  are presented in (b) for  $t_d = 400 \mu\text{sec}$ ; in both examples,  $N_{PB} = 3$ . The shapes of the loop signals (proportional to beta) in (a) and (b) and the triple-probe current and temperature signals in (b) are seen to resemble the beta, density, and temperature traces, respectively, of the simulation shown in Fig. 5(b); in fact, even the relative times of the peaks of the loop signal and the triple-probe current and temperature signals of (b) are in the same order (temperature-beta-density). However, the Langmuir probe trace in (a) is highly oscillatory. The violent fluctuations on the leading edge are interpreted as fluctuations in the space (and floating) potentials of the plasma caused by the ringing preionizer. The smaller ripples later in time are interpreted as potential fluctuations caused by the modulation of the crowbarred theta-pinch current, evident in Fig. 3(b). These interpretations are supported by the facts that the oscillations are not reflected on the loop trace and are much smaller on the triple-probe current. Because of the latter, the triple-probe data is used to obtain the densities in this section.

As was seen from the simulation results of Section III.B,  $n_{\beta\max}$  and  $T_{\beta\max}$  both decrease with  $b_S \equiv B_S/B_{TP}$  (for fixed initial conditions). Hence, increasing the theta-pinch field (increasing  $N_{PB}$ ) to achieve higher betas and temperatures may be offset by increasing decompression into a fixed solenoid field. To examine this question, a number of shots were taken with  $t_d = 300 \mu\text{sec}$  for  $N_{PB} = 2, 3, \text{ and } 4$ . ( $B_{TP} \approx 1.2 \text{ T}, 1.7 \text{ T}, \text{ and } 2.2 \text{ T}$ , respectively). The data is plotted versus  $B_{TP}$  in Fig. 10, where  $\langle\beta\rangle_{\max}$  is the peak beta averaged over the cross section of the chamber.

We see in Fig. 10 (a) that within experimental error,  $\langle\beta\rangle_{\max}$  is relatively independent of  $N_{PB}$ ; this is in contrast to the simulation results of Fig. 6, which, for a constant value of  $\beta_0$ , predict a monotonically increasing  $\beta_{\max}$  with  $B_{TP}/B_S$ . This is attributable to the drop in  $n_{\beta\max}$  with  $B_{TP}$ , seen in Fig. 10(c). From the simulation results of Fig. 6,  $n_{\beta\max} \equiv n_{\beta\max}/n_0$  was found to scale somewhat slower than  $b_S^{3/4}$ , i.e.,  $b_S^{2/3}$ . The temperature in a long theta-pinch at peak compression scales roughly as  $B_{TP}^{4/3}$  (for  $\beta_0$  a constant)<sup>16</sup>; hence,  $n_0 \propto B_{TP}^{2/3} \propto b_S^{-2/3}$ . Thus,  $n_{\beta\max} = n_{\beta\max} n_0 \propto b_S^{2/3} b_S^{-2/3} \approx \text{constant}$ . The drop in  $n_{\beta\max}$  with  $B_{TP}$  seen in Fig. 10 (c) is not understood but may be due to increasing amounts of plasma striking the chamber wall upon exiting the theta-pinch.

$T_e(\beta_{\max})$  for  $N_{PB} = 3$  and  $t_d = 400 \mu\text{sec}$  was measured with the triple-probe to be about 8 eV (as seen in Fig. 9 (b)). Coupled with an average  $n_{\beta\max}$  of about  $8 \times 10^{14} \text{ cm}^{-3}$ , the ion-electron energy equilibration time<sup>17</sup> is of order 1  $\mu\text{sec}$ ; thus  $T_i = T_e \equiv T$ . The values of  $T_{\beta\max}$  in Fig. 10 (d) were obtained from the ratio  $\langle\beta\rangle/n_{\beta\max}$  relative to that for  $N_{PB} = 3$  and  $t_d = 400 \mu\text{sec}$ . (This assumes that the plasma cross section does not itself scale with  $N_{PB}$  or  $t_d$ .)  $T_{\beta\max}$  is seen to

increase monotonically with  $B_{TP}$ . The simulation results of Fig. 6 indicate that  $T_{\beta_{max}} \equiv T_{\beta_{max}}/T_0$  scales roughly as  $b_S^{1/2}$  for  $\beta_0$  constant. For  $T_0 \propto B_{TP}^{4/3} \propto b_S^{-4/3}$ , this implies  $T_{\beta_{max}} = T_{\beta_{max}} T_0 \propto b_S^{-5/6} \propto B_{TP}^{5/6}$ . A plot of this function, normalized to intersect the plot of  $T_{\beta_{max}}$  at  $B_{TP} = 0.17 T$ , is shown as the dashed curve of Fig. 10(d). The agreement between the two curves is satisfactory.

The simulations also indicate that  $v_{\beta_{max}} \equiv v_{\beta_{max}}/v_{i0}$  is relatively independent of both  $b_S$  and  $\beta_0$ ; thus,  $v_{\beta_{max}} \propto v_{i0} \propto \sqrt{T_0}$ . For  $T_0 \propto B_{TP}^{4/3}$ , this yields  $v_{\beta_{max}} \propto B_{TP}^{2/3}$ . A plot of this function, normalized to intersect the experimental curve of  $v_{\beta_{max}}$  at  $B_{TP} = 1.7 T$ , is shown as the dashed curve in (b). Again, the agreement is satisfactory. Finally, the solid curves for  $T_{\beta_{max}}$  and  $v_{\beta_{max}}$  are used to obtain the Mach number, which is also plotted in (b);  $M_{\beta_{max}}$  is seen to increase slightly with  $B_{TP}$ . From the numerically determined scalings of  $v_{\beta_{max}}$  and  $T_{\beta_{max}}$  above, one obtains  $M_{\beta_{max}} \propto v_{\beta_{max}} / \sqrt{T_{\beta_{max}}} \propto B_{TP}^{1/4}$ . This function is plotted as the dashed curve for  $M_{\beta_{max}}$  in (b). While the scaling is correct, the experimental values of  $M_{\beta_{max}}$  are much lower than the simulation results. A possible explanation of this discrepancy is hinted at in Fig. 6; we see that as  $\beta_0 \rightarrow 1$ ,  $T_{\beta_{max}}$  dramatically increases and  $M_{\beta_{max}}$  decreases. Thus, if the plasma is actually created in a field-reversed configuration, as is not unusual in theta-pinches which use a ringing discharge to preionize,<sup>18</sup> axial expansion and the resulting cooling would be delayed until the reversed field dissipated. (Because of the high collisionality of the plasma, this would happen fairly quickly.) Since the simulations indicate that  $v_{\beta_{max}}$  is relatively independent of  $\beta_0$ , such a situation would result in lower Mach numbers.

## B. Injection into multiple mirrors ( $R_m > 1$ )

We now examine qualitatively the predictions of the simulations as to shock formation. A necessary condition for shocks to exist is that the flow through the mirrors be collisional, i.e., that  $\lambda_d \equiv v\tau_i \ll \ell_m$  where  $\tau_i$  is the ion-ion scattering time<sup>17</sup> and  $\ell_m$  is the scale length of the mirror field. To reduce  $\lambda_d$ , the experiments of this section were performed with  $t_d = 450 \mu\text{sec}$  and the theta-pinch was operated in the ringing mode, producing a denser, colder plasma. In addition, to lower the ratio  $B_{TP}/B_S$  (to increase  $b_S$ ) so that the mirror fields for  $R_m \leq 4$  were comparable to the theta-pinch field, only two the theta-pinch capacitors were used ( $b_S \approx 0.15$ ). Under these conditions, the outputs of  $DL_{01}$  and a Langmuir probe at  $M_{01}$  for  $R_m = 1$  are as shown in Fig. 11 (a) (note the change in the time scale). From  $DL_{01}$ ,  $\langle \beta \rangle_{\text{max}} \approx 0.021$  and  $v_{\beta\text{max}} \approx 6.6 \text{ cm}/\mu\text{sec}$ . From the triple-probe now located at  $M_{12}$ ,  $T_{\beta\text{max}} \approx 6 \text{ eV}$ . Thus,  $n_{\beta\text{max}} \approx 9 \cdot 10^{14} \text{ cm}^{-3}$ . For these values,  $\lambda_d \approx 0.2 \text{ cm}$ , such that shocks, if they occur for  $R_m > 1$ , would be clearly recognizable. (Also shown in Fig. 11 (a) is the output of the velocity-stagnation probe aimed downstream at  $M_{01}$ , which is negligible, as expected for  $R_m = 1$ .)

### 1. Results without quadrupole fields

Because of the relatively low temperature and the corresponding slow growth rates for MHD instabilities with  $R_m > 1$ , as well as the possibilities of wall stabilization and line-tying, we can perform the experiment without quadrupole stabilizing fields. Signals from the same diagnostics as in (a) are shown in Fig. 11(b) for  $R_m = 3$ . The plasma appears stable (no "dumps" on the probe or loop signals) and secondary peaks occur on the traces well after the peak signals. We

now show why these secondary peaks represent a shock propagating upstream from  $T_1$ .

We see that the pulses on the Langmuir probe and velocity-stagnation probe signals occur earlier than that of the loop signal. Since  $DL_{01}$  is about 12 cm upstream of the probes, this implies that the disturbance moves upstream, as a shock would; from time-of-flight, the velocity is 1-1.5 cm/ $\mu$ sec. The pulse on the velocity-stagnation probe signal indicates that the drift velocity abruptly slows, as it would after passage of a shock front. The slight difference in the times of the pulses on the velocity-stagnation probe (located approximately 2 cm off axis) and the Langmuir probe occurs because the velocity of the disturbance depends on radius, as determined with an array of probes at differing radii. The non-planar nature of the disturbance qualitatively explains the relatively thick front implied by the loop signal. (Similar loop and probe signals were seen by Uchida et al.<sup>1</sup>) The larger pulse on the loop signal relative to that on the Langmuir probe signal indicates that the temperature also rises, as it does after passage of a shock front. (An array of three probes at different radii, indicates the plasma radius increases somewhat after passage of the disturbance, but not enough to account for the large pulse on the loop signal.)

It is evident in comparing the Langmuir probe and loop signals of Figs. 11 (a) and 11 (b) that the primary peaks are smaller and decay faster in the latter figure. This effect also appears in the simulation results of Figs. 5 (b) and 7 (b), due to choking of the flow by a shock already formed upstream of  $T_0$ . That this indeed occurs is evident in Fig. 12 (a), which shows the signal from a Langmuir probe

at  $M_{B0}$  (see Fig. 1). The pulse is seen to occur prior to that in Fig. 11 (b). Shown in Fig. 12 (b) are the outputs of the triple-probe at  $M_{12}$ , indicating a shock forms in  $T_2$ ; a definite increase in temperature occurs after passage of the shock. The rapid decay of the primary density peak can be attributed to the choking of the flow by the shocks in  $T_0$  and  $T_1$ .

To be more quantitative, the secondary peaks in Fig. 11 (b) are examined with respect to the Rankine-Hugoniot conditions.<sup>1</sup> For a drift velocity of 3.2 cm/ $\mu$ sec and a temperature of  $(1.7 \pm 0.3)$  eV just prior to the shock, and a shock speed of  $(1.25 \pm 0.25)$  cm/ $\mu$ sec, the density and temperature should increase by the factors  $2.2 \pm 0.16$  and  $2.0 \pm 0.15$ , respectively. Thus, the pressure (proportional to beta) should increase by the factor  $4.4 \pm 0.5$ . The density increase implied by the Langmuir probe current in Fig. 11 (b) is computed to be  $1.9 \pm 0.2$ , agreeing satisfactorily with the predicted value. In addition, the increase in the loop signal can be accounted for by a pressure (beta) increase of about 4.4 and a moderate increase in the plasma radius. Although the signals of Fig. 12 (b) are at  $M_{12}$ , the density and temperature both increase by approximately a factor of two. These results indicate that the shocks are not particularly strong; for a strong shock the density should increase by a factor of four.

As in the simulation results of Fig. 8, the time of shock formation is studied as a function of  $R_m$ . The signals from  $DL_{01}$  and a Langmuir probe at  $M_{01}$  are shown in Figs. 13 (a), (b), and (c) for  $R_m = 2, 3,$  and  $4,$  respectively. (The signals in (b) are taken from Fig. 11 (b).) As expected, the shocks occur earlier as  $R_m$  is increased, while the jumps on

the loop signals are greater; the latter is explained by the fact that at earlier times the plasma is more energetic.

## 2. Results with quadrupole fields

A hint of instability is evident on the probe signal of Fig. 13 (c); other experiments using an array of probes at different radii indicate the plasma is somewhat off-center (no dumps are observed, however). Since quadrupole fields are essential for operation of the device at higher temperatures (at least in its present configuration), it is important to examine their effects on shock formation. As a first guess, one might expect these to be minimal since the quadrupoles impart only transverse components of magnetic field-- $R_m$  is not affected.

The signals from  $DL_{01}$  and a Langmuir probe at  $M_{01}$  are shown in Figs. 14 (a) and 14 (b) for  $R_m = 3$  and  $R_m = 4$ , respectively, with the quadrupole fields at their design levels. (Also shown in (a) is the output of the velocity-stagnation probe.) Comparison with Figs. 11 (b) and 13 (c), respectively, reveals that the secondary peaks occur later and are much weaker (especially on the loop signals). In addition, the increase in temperature at  $M_{12}$ , as measured by the triple-probe, is minimal.

An explanation for the reduced secondary peaks when the quadrupoles are energized is the following: The quadrupoles map a circular flux tube in a midplane to an ellipse in a mirror. Under design conditions, a field line defined by the intersection of the chamber wall and the major axis of the ellipse in a mirror throat is at a radius  $r_{max}$  of only 1.7-1.8 cm at a midplane. Plasma outside this radius strikes the wall upon flowing into a mirror region. Since the plasma

radius with  $R_m = 1$  was measured at somewhat greater than 2 cm, a significant portion of the plasma with  $R_m > 1$  strikes the wall before reaching a mirror. Assuming that a shock is formed in a mirror throat over the entire cross section of the plasma, and that the shock propagates upstream along a flux tube, one concludes that the plasma lying outside of  $r_{\max}$  does not participate in shock formation and subsequent thermalization; this would explain the smaller secondary peaks on the loop signals. Radial diffusion and subsequent weakening of the shock front would explain the smaller secondary peaks on the probe signals.

## V. CONCLUSION

The principal goal of this work was to understand the process by which a collisional plasma injected into one end of a multiple-mirror configuration is trapped. To this end, a fluid simulation code was developed. The results pointed out, first, the significant conversion of thermal energy in the theta-pinch source to drift energy in the multiple-mirror device. The scaling of plasma parameters -- density, temperature, drift velocity, etc. -- were examined in a uniform solenoid ( $R_m = 1$ ) as a function of the ratio of the solenoid field to the peak theta-pinch field  $b_S$ . It was found that the density, temperature, and drift velocity increased with  $b_S$  while the beta and Mach number decreased. Results for injection into mirrors ( $R_m > 1$ ) indicated that the drift energy is thermalized by shocks which form sequentially in the mirror throats, beginning in the mirror nearest the source, and propagate upstream. The shocks were found to form later as the mirror fields were reduced, until a "cutoff" was reached in the magnitude of

the mirror fields below which shocks did not form.

Experiments were performed first in a fixed solenoid field ( $R_m = 1$ ) in which the plasma parameters were studied as a function of the peak theta-pinch field. The scalings of temperature and drift velocity were well described by the simulation results for  $R_m = 1$ , assuming that the peak temperature in the theta-pinch was proportional to  $B_{TP}^{4/3}$ . Experiments using a highly collisional plasma were next performed with  $R_m > 1$  in which the numerically predicted characteristics of shock formation and propagation were verified. In addition, it was found that quadrupole stabilizing fields interfered with shock-thermalization.

#### ACKNOWLEDGMENTS

Appreciation is extended to Professor W.B. Kunkel for his insightful contributions and to J. Benasso, Dr. N. Benjamin, B. Bingham, Dr. C. Hartman, and D. Price for their technical assistance.

This research was supported by DOE Contract DE-AT03-76ET53059 and NSF Grant ECS 8104561.

## REFERENCES

- <sup>1</sup>T. Uchida, K. Miyamoto, J. Fujita, S. Kawasaki, N. Inoue, Y. Suzuki, and K. Adati, *Nucl. Fusion* 8, 263 (1968).
- <sup>2</sup>T. Uchida, K. Miyamoto, J. Fujita, N. Inoue, Y. Suzuki, and K. Adati, *Nucl. Fusion* 11, 441 (1971).
- <sup>3</sup>W.R. Kramer and J.G. Siambis, *Phys. Fluids* 15, 1652 (1972).
- <sup>4</sup>C. Leloup and R. Taussig, *Nucl. Fusion* 8, 4 (1968).
- <sup>5</sup>S. Hamada, I. Kawakami, and M. Sato, *J. Phys. Soc. Jap.* 25, 542 (1968).
- <sup>6</sup>B.W. Johnson and J.G. Siambis, *Plasma Phys.* 15, 369 (1973).
- <sup>7</sup>J.C. Riordan, A.J. Lichtenberg, and M.A. Lieberman, *Nucl. Fusion* 19, 21 (1979).
- <sup>8</sup>F.F. Chen, in Plasma Diagnostic Techniques, edited by R.H. Huddleston and S.L. Leonard (Academic Press, New York, 1965), p. 113.
- <sup>9</sup>Sin-Li Chen and T. Sekiguchi, *J. Appl. Phys.* 36, 2363 (1965).
- <sup>10</sup>F. Waelbroeck, C. Leloup, J.P. Poffé, P. Evrard, R. Der Agobian, and D. Véron, *Nucl. Fusion Suppl. Part 2*, 675 (1962).
- <sup>11</sup>J.G. Laframboise, University of Toronto Institute for Aerospace Studies Report No. 100, 1966.
- <sup>12</sup>R.V. Bravenec, Ph.D. dissertation, University of California, Berkeley, 1982.
- <sup>13</sup>J. VonNeumann and R.D. Richtmyer, *J. Appl. Phys.* 21, 232 (1950).
- <sup>14</sup>N.K. Madsen and R.F. Sincovec, *ACM Trans. on Math. Soft.* 5, 326 (1979).
- <sup>15</sup>K.P. Stanyukovich, Unsteady Motion of Continuous Media (Pergamon Press, New York, 1960).
- <sup>16</sup>R. Mewe, *Z. Naturforsch.* 25a, 1803 (1970).
- <sup>17</sup>S.I. Braginskii, in Reviews of Plasma Physics, edited by M.A. Leontovich (Consultants Bureau, New York, 1965), Vol. 1, p. 205.
- <sup>18</sup>W.B. Jones and R.D. Miller, *Phys. Fluids* 11, 1550 (1968).

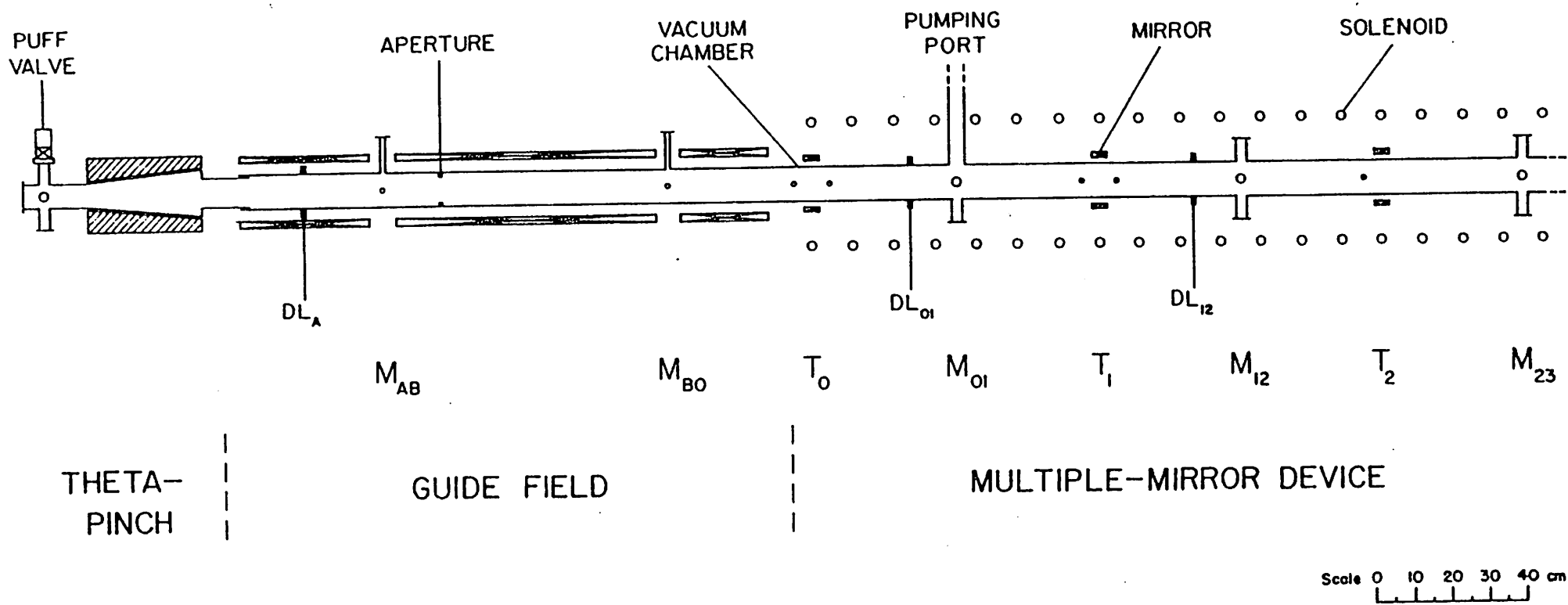


FIG. 1. The experimental apparatus.

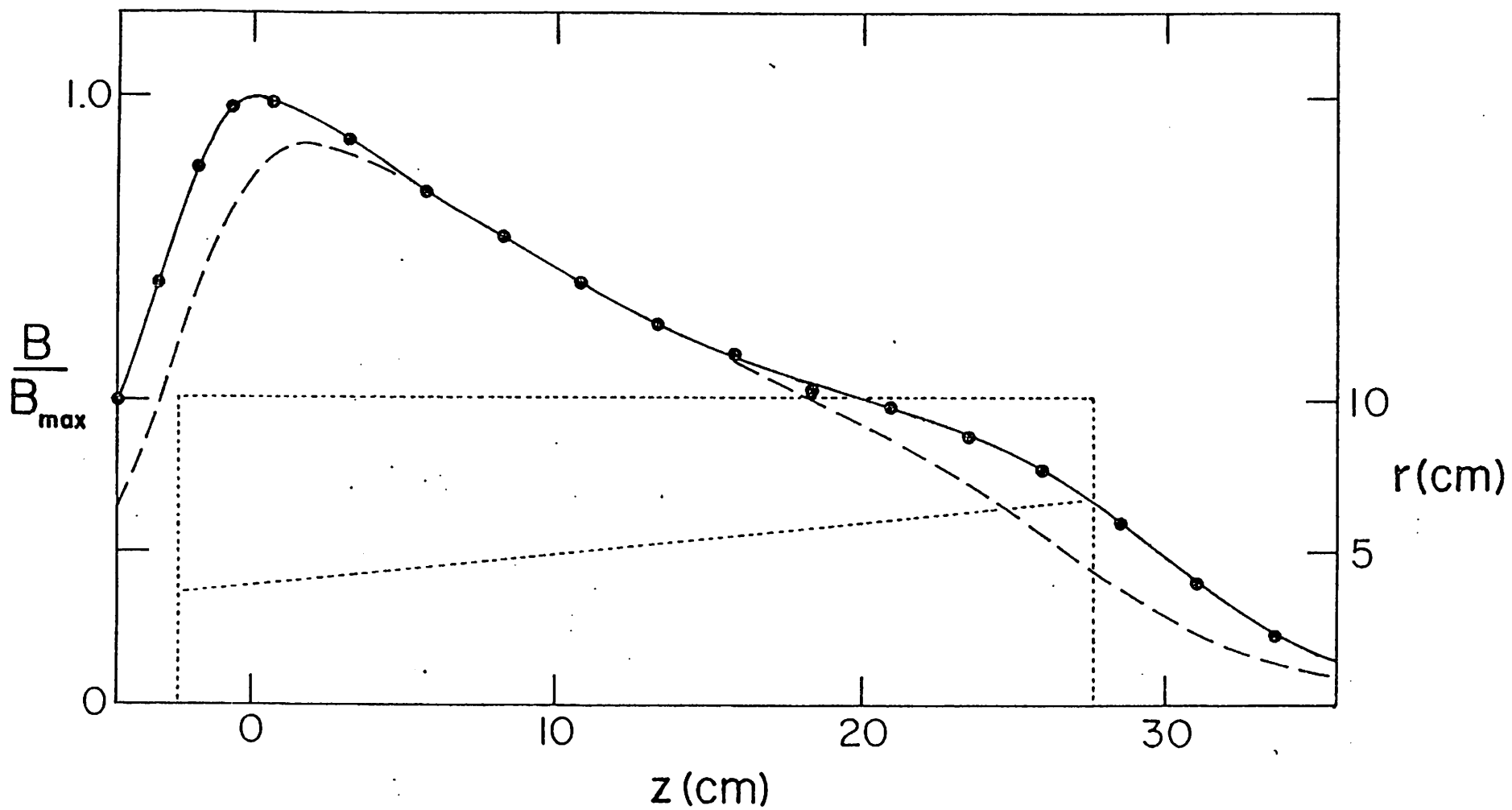
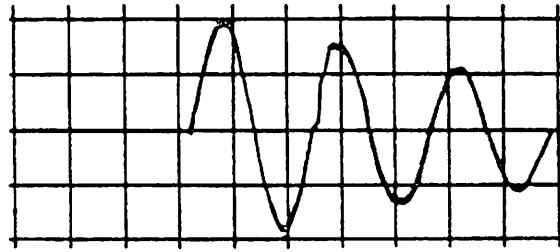
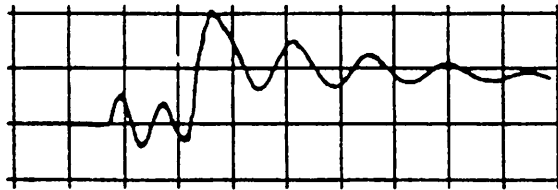


FIG. 2. Axial magnetic field profile in the theta-pinch coil as measured (solid curve with data points) and calculated (dashed curve). A cross section of the coil is shown as the dotted lines.



(a)



(b)

FIG. 3. Theta-pinch discharge waveforms in (a) ringing mode and (b) preionized/crowbarred mode for  $N_{PB} = 3$  and  $t_d = 300 \mu\text{sec}$ . Time scale:  $2 \mu\text{sec/div}$ .

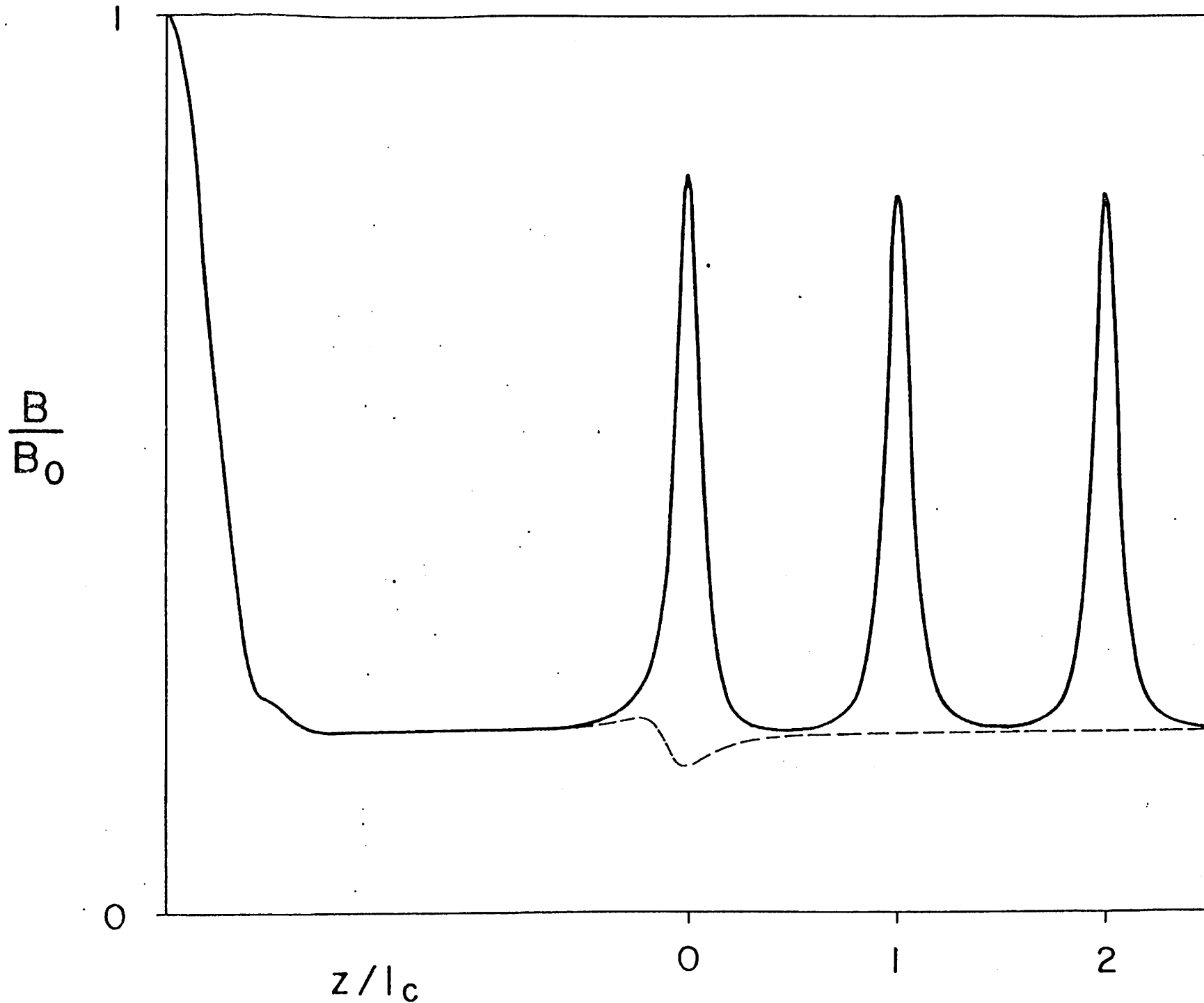


FIG. 4. Normalized magnetic field profiles used in the simulations with  $R_m = 4$  (solid curve) and  $R_m = 1$  (dashed curve).

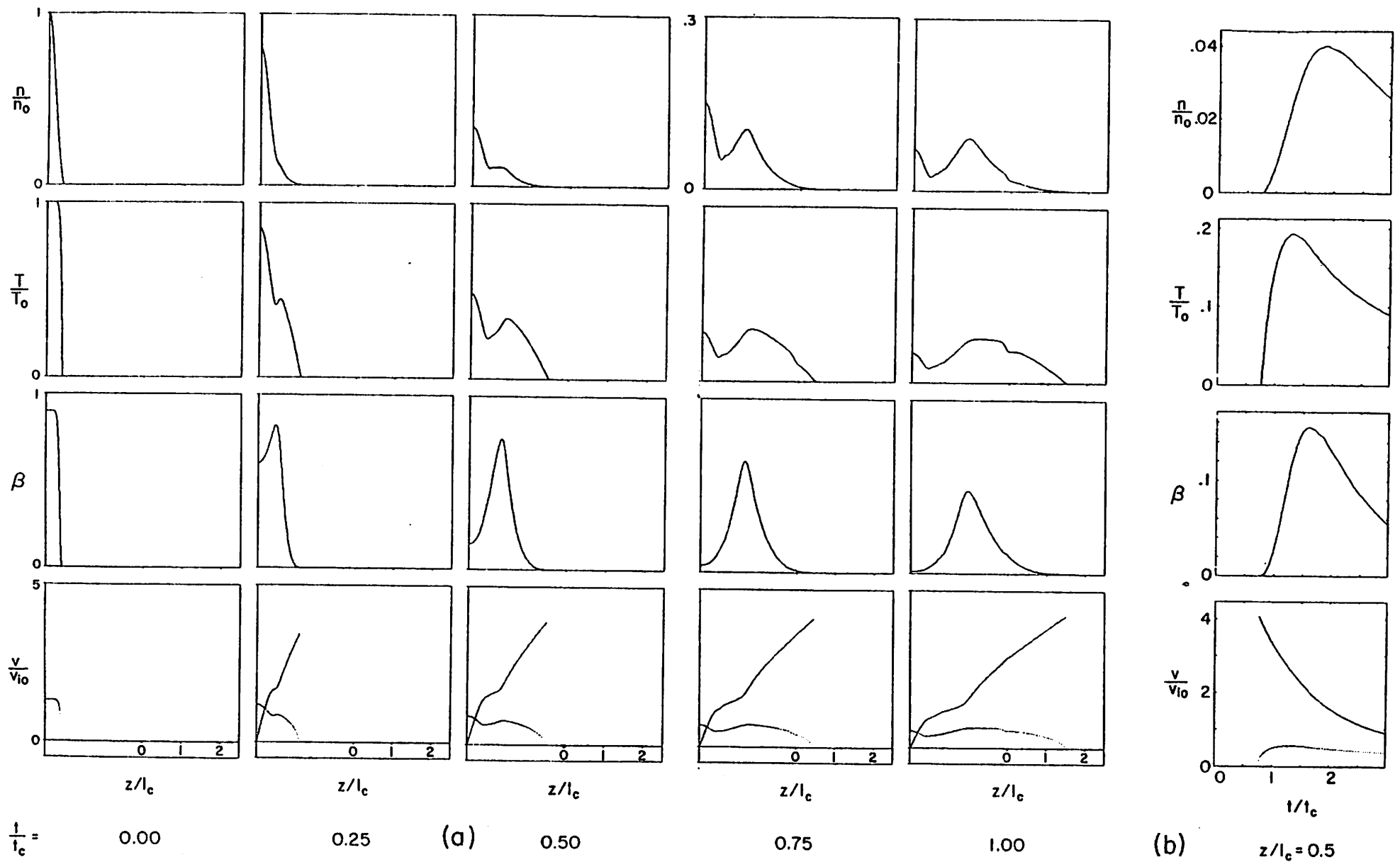


FIG. 5. Simulation results for  $R_m = 1$  with  $b_S = 0.2$  and  $\beta_0 = 0.9$ . Top to bottom: Normalized density, normalized temperature, plasma beta, and normalized drift velocity ( $v_{i0} \equiv (2kT_0/m_i)^{1/2}$ ). Dotted curves in plots of  $v/v_{i0}$  are plots of normalized sound speed  $v_s/v_{i0} \equiv (5T/3T_0)^{1/2}$ . (a) Spatial profiles at normalized time intervals of 0.25 ( $t_c \equiv \ell_c/v_{i0}$ ). (b) Time profiles at  $z/\ell_c = 0.5$ .

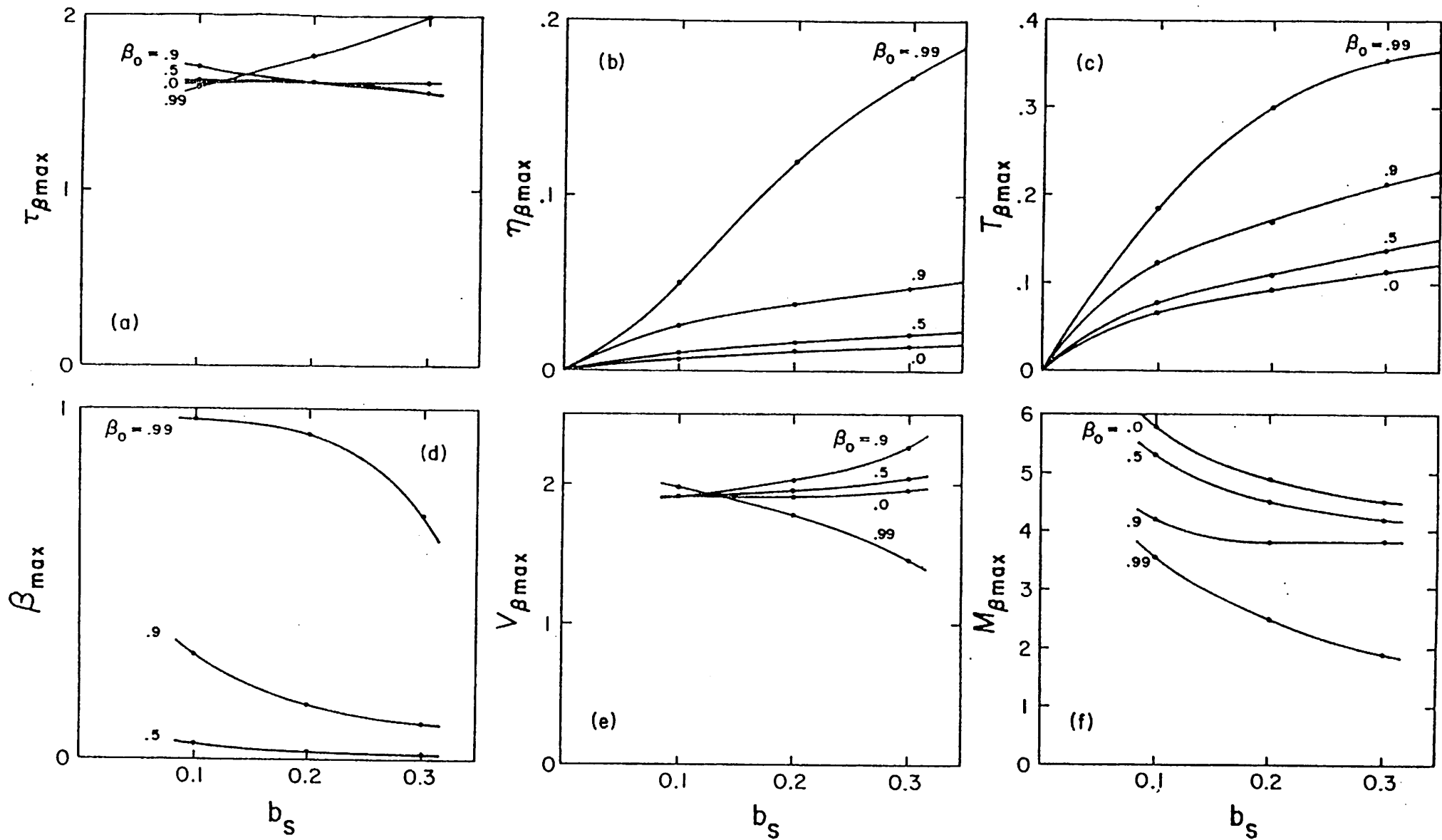


FIG. 6. Simulation results with  $R_m = 1$  for plasma parameters at the time of peak beta at  $z/\lambda_c = 0.5$  versus the normalized solenoid field  $b_s$  and initial beta  $\beta_0$ . (a) Normalized time of peak beta, (b) normalized density, (c) normalized temperature, (d) peak beta, (e) normalized drift velocity, (f) Mach number.

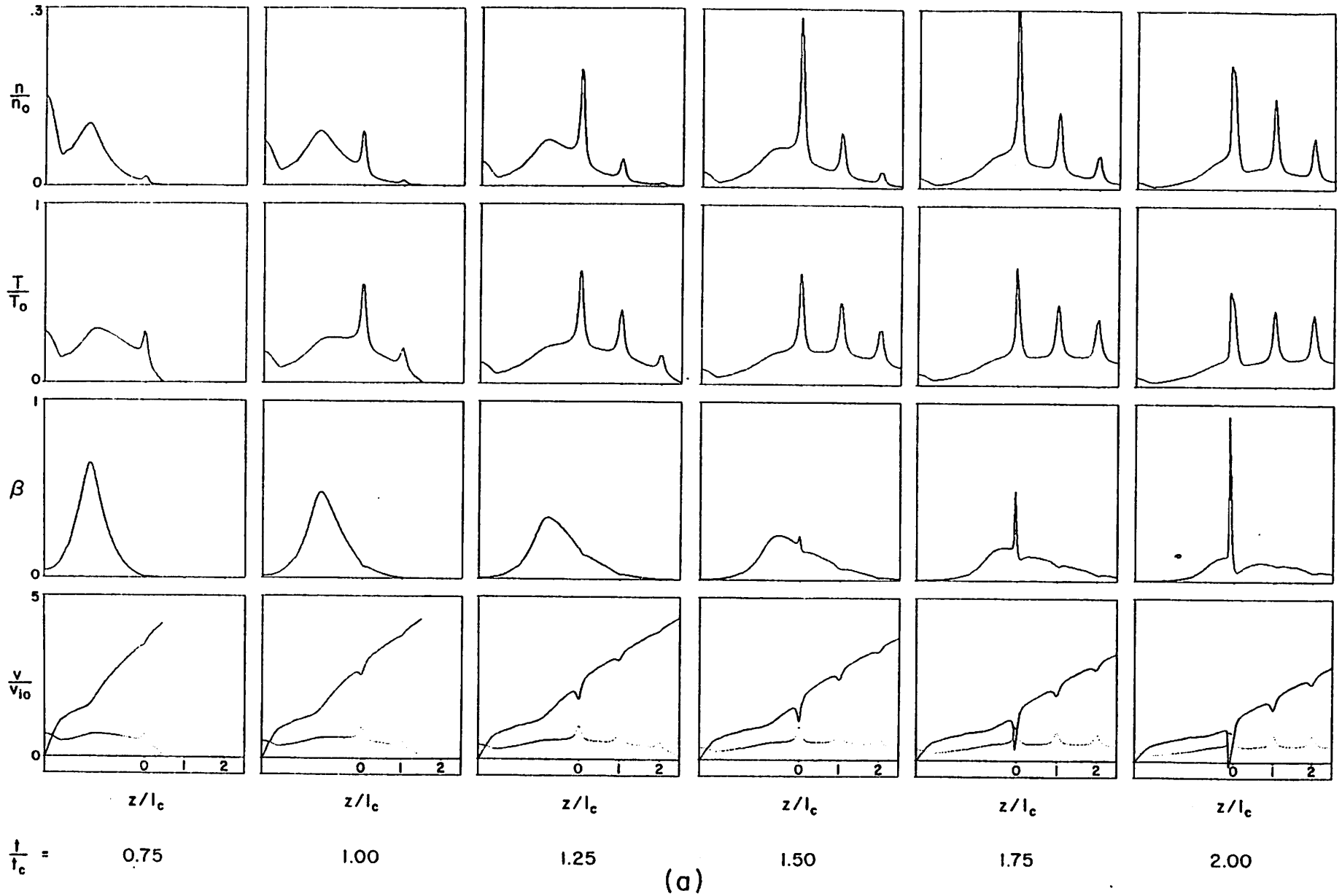
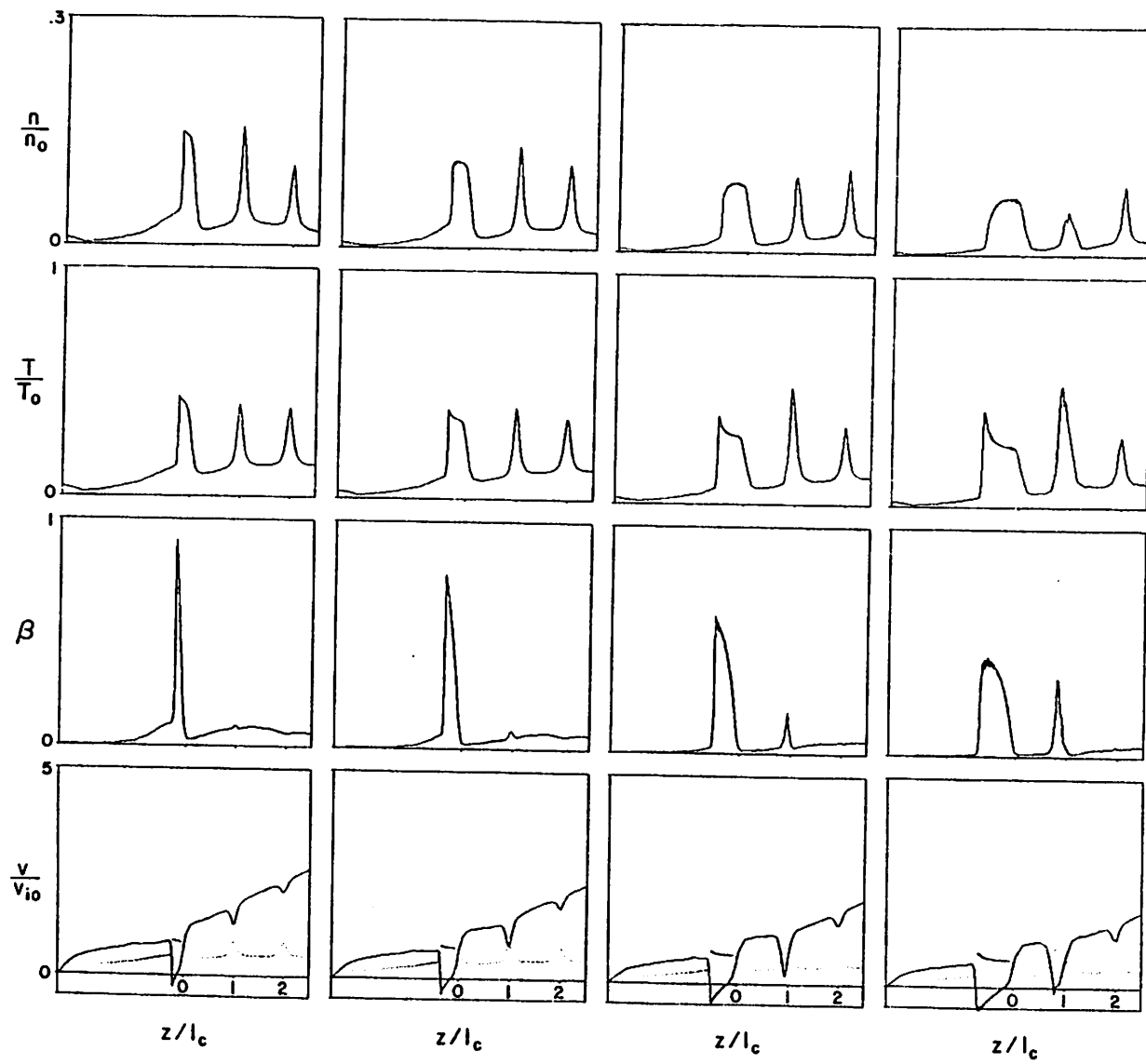
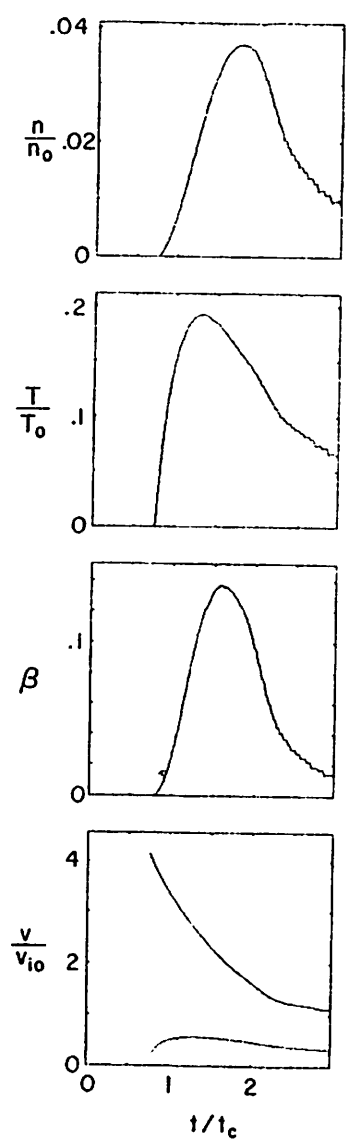


FIG. 7. Simulation results for  $R_m = 4$  with  $b_s = 0.2$  and  $\beta_0 = 0.9$ . Top to bottom: Normalized density, normalized temperature, plasma beta, and normalized drift velocity ( $v_{i0} = (2kT_0/m_i)^{1/2}$ ). Dotted curves in plots of  $v/v_{i0}$  are plots of normalized sound speed  $v_s/v_{i0} \equiv (5T/3T_0)^{1/2}$ . (a) Spatial profiles at normalized time intervals of 0.25 ( $t_c \equiv \ell_c/v_{i0}$ ). (b) Time profiles at  $z/\ell_c = 0.5$ .



$t/t_c =$  2.25 2.50 (a) cont. 2.75  $t/t_c = 3.00$



(b)  $z/l_c = 0.5$

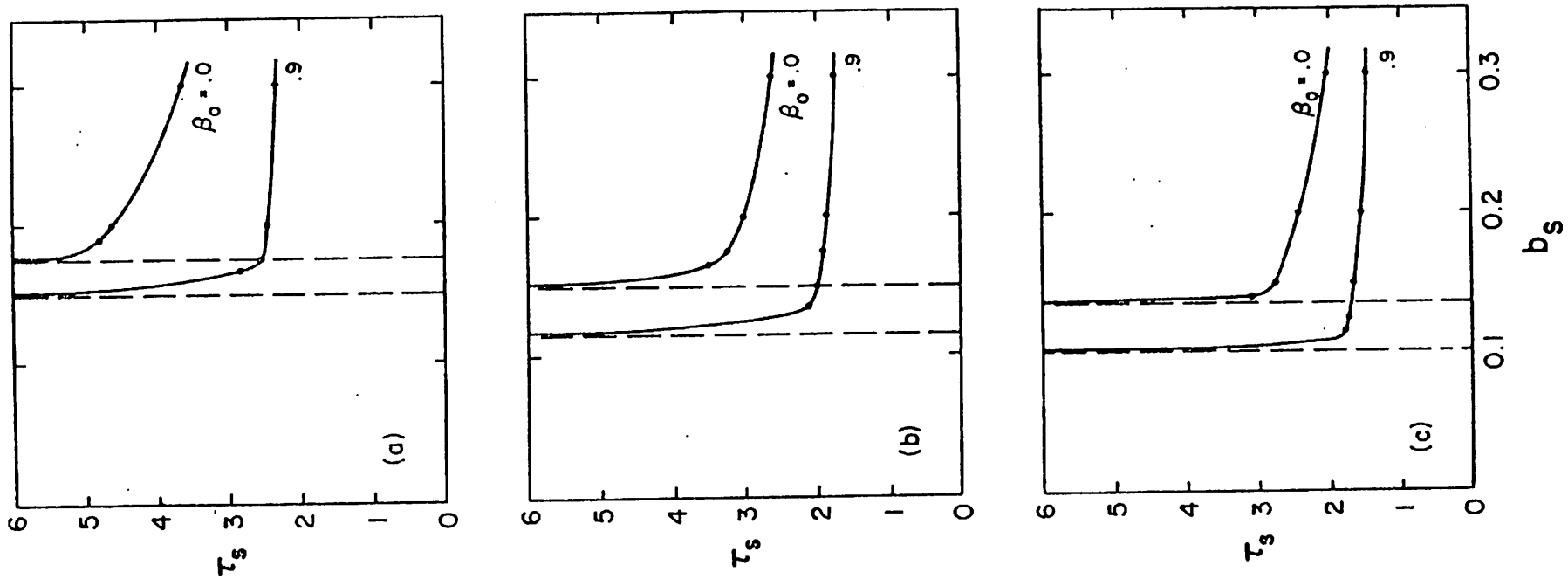
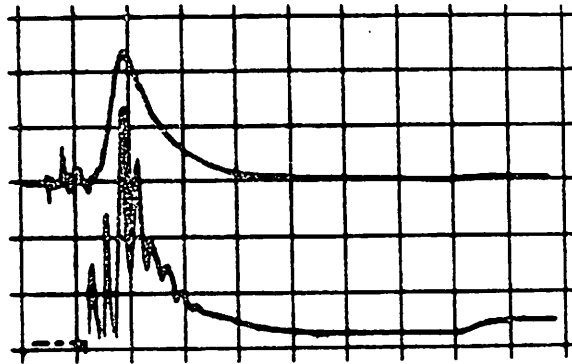
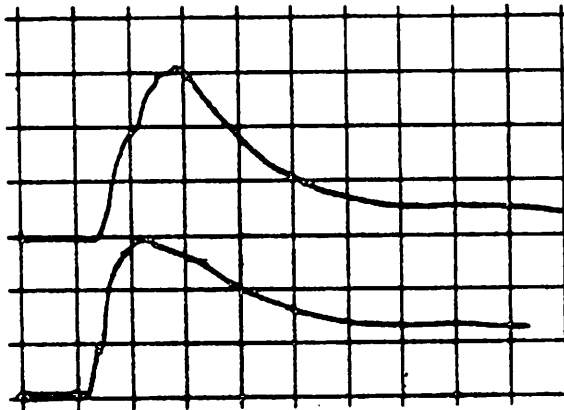
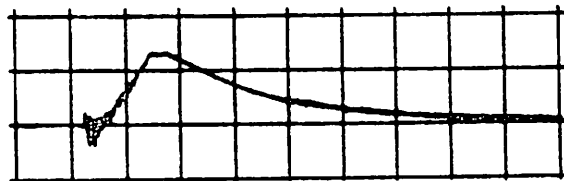


FIG. 8. Simulation results with  $R_m =$  (a) 2, (b) 3, and (c) 4 for the normalized shock-formation time in the first mirror versus the normalized solenoid field  $b_s$  and initial beta  $\beta_0$ .



(a)



(b)

FIG. 9. Signals at  $M_{01}$  with  $R_m = 1$  and  $N_{pg} = 3$  for (a)  $t_d = 300 \mu\text{sec}$  and (b)  $t_d = 400 \mu\text{sec}$ . Top traces in (a) and (b) are diamagnetic loop voltage (50 mV/div), bottom trace in (a) is Langmuir probe current (0.5 A/div), and bottom traces in (b) are triple-probe current and electron temperature (0.5 A/div and 2.8 eV/div, respectively). Time scale: 10  $\mu\text{sec}/\text{div}$ .

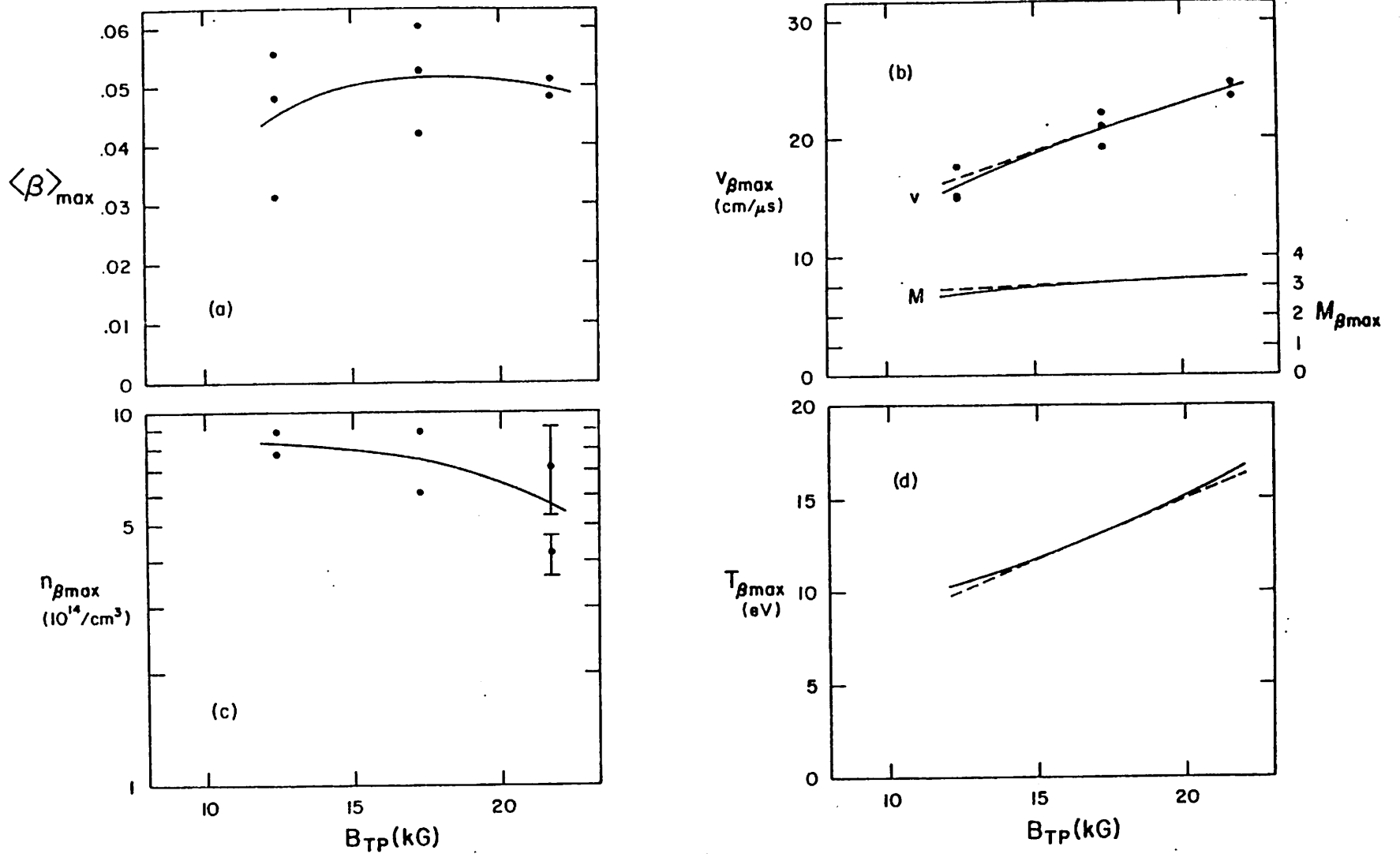
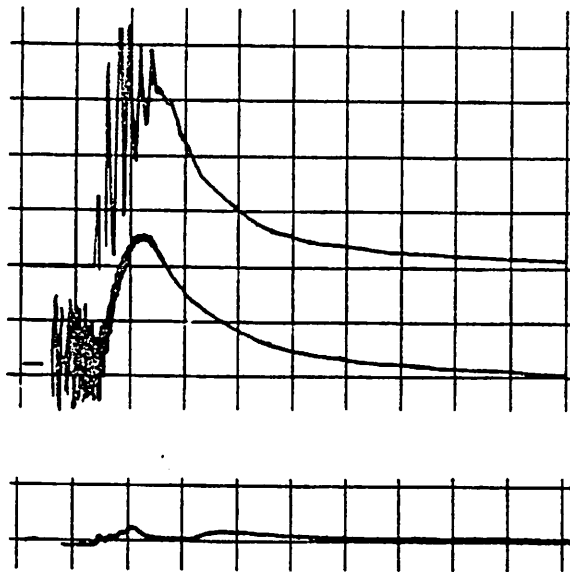
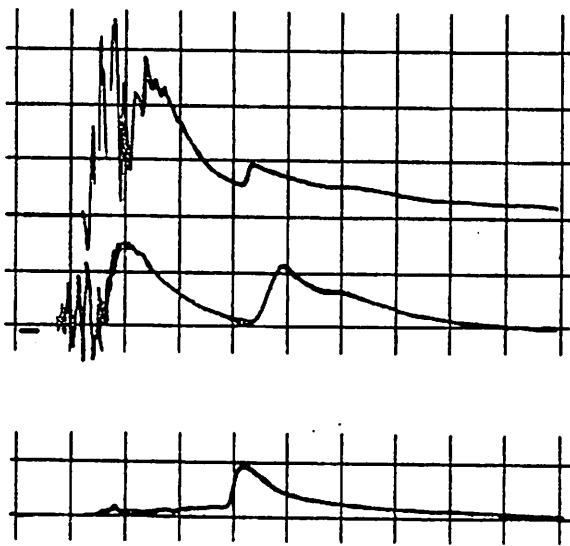


FIG. 10. Experimental data at  $M_{01}$  with  $R_m = 1$  and  $t_d = 300 \mu\text{s}$  for plasma parameters at the time of the peak diamagnetic loop signal versus peak theta-pinch field. (a) Peak chamber-averaged beta, (b) drift velocity  $v$  and Mach number  $M$ , (c) density, (d) temperature. Dashed lines represent scalings predicted by simulations.

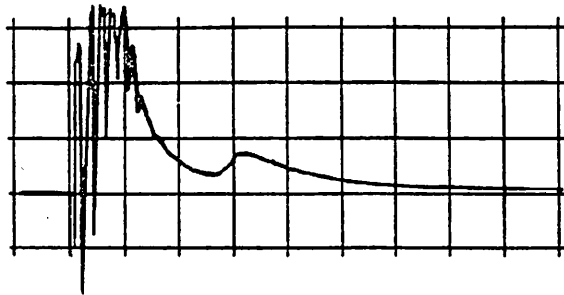


(a)



(b)

FIG. 11. Signals at  $M_{01}$  with (a)  $R_m = 1$  and (b)  $R_m = 3$  (no quadrupoles) from (top to bottom) Langmuir probe (0.5 A/div), diamagnetic loop (20 mV/div), and velocity-stagnation probe (0.7 A/div). Time scale: 20  $\mu$ sec/div.  $N_{PB} = 2$  (ringing mode),  $t_d = 450 \mu$ sec.

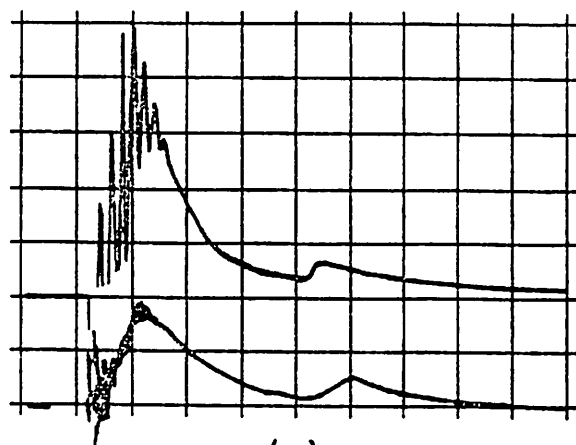


(a)

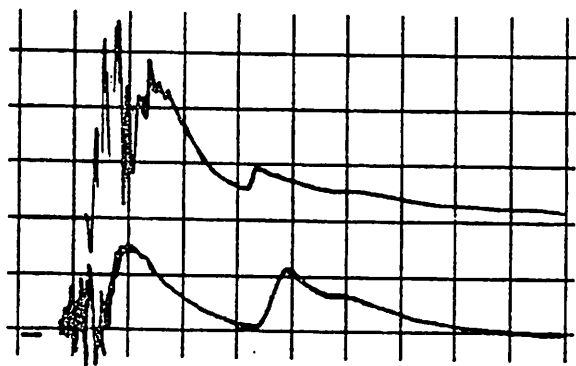


(b)

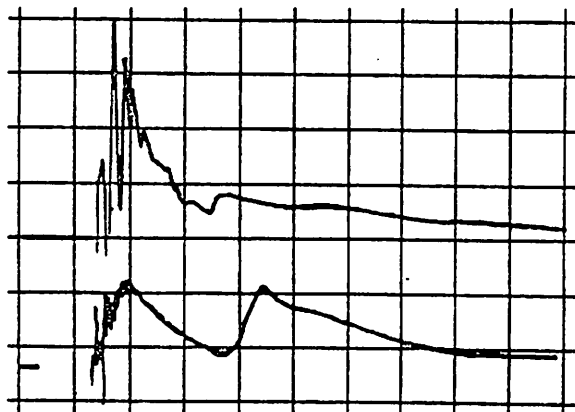
FIG. 12. (a) Langmuir probe current (1.0 A/div) at  $M_{B0}$  and (b) triple-probe current and electron temperature (0.5 A/div and 2.8 eV/div, respectively) at  $M_{12}$  for  $R_m = 3$  (no quadrupoles). Time scale: 20  $\mu\text{sec}/\text{div}$ .  $N_{PB} = 2$  (ringing mode),  $t_d = 450 \mu\text{sec}$ .



(a)

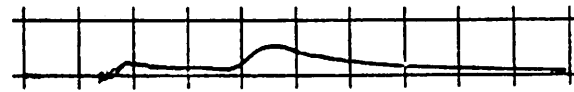
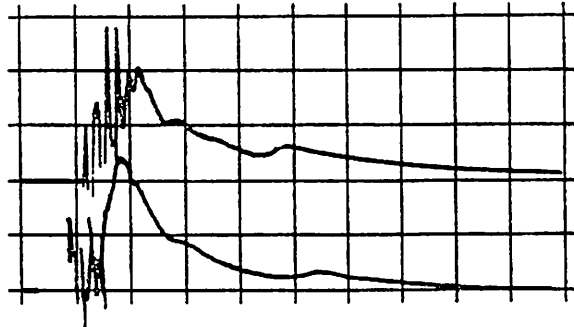


(b)

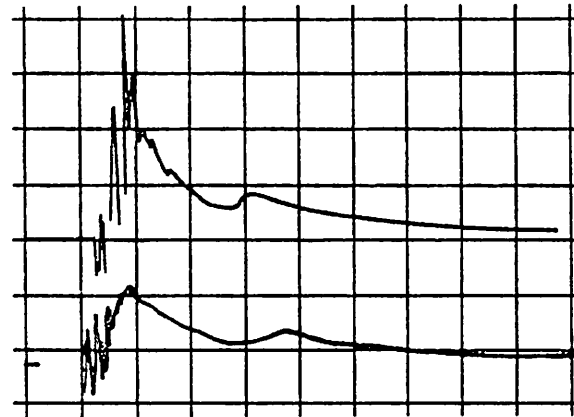


(c)

Fig. 13. Signals at  $M_{01}$  from Langmuir probe (0.5 A/div) and diamagnetic loop (20 mV/div) for  $R_m =$  (a) 2, (b) 3, and (c) 4 (no quadrupoles). Time scale: 20  $\mu$ sec/div.  $N_{PB} = 2$  (ringing mode),  $t_d = 450 \mu$ sec.



(a)



(b)

FIG. 14. Signals at  $M_{01}$  for (a)  $R_m = 3$  and (b)  $R_m = 4$  (with quadrupoles) from Langmuir probe (0.5 A/div) and diamagnetic loop (20 mV/div). Also shown in (a) is output of velocity-stagnation probe (0.7 A/div). Time scale: 20  $\mu\text{sec}/\text{div}$ .  $N_{PB} = 2$  (ringing mode),  $t_d = 450 \mu\text{sec}$ .